Materials Advances

ROYAL SOCIETY OF CHEMISTRY

PAPER

View Article Online
View Journal | View Issue

Cite this: *Mater. Adv.*, 2025, **6**, 5726

Isoniazid-loaded multicore magnetic nanoparticles as a facile intervention for combating mycobacterial infection

Lipsa Leena Panigrahi,[a] Ashirbad Sarangi,[a] Bhabani Shankar Das,[ad] Shashank Shekhar,[b] Debapriya Bhattacharya[c] and Manoranjan Arakha *[a]

A hybrid first-line tuberculosis antibiotic conjugated programable magnetic nanoplatform for application in precision therapeutics for treating tuberculosis (TB) is described. Here the citrate anion grafted multicore magnetic nanoparticles (MC-IONPs) enable the precise delivery of isoniazid (INH). This approach promotes specificity and synergistically improves the accumulation of isoniazid on the bacterial membrane interface, thus avoiding the need for higher doses for the treatment. Despite the wide use of isoniazid, there has been no optimal dose established for the treatment of TB, which has led to inadequacy in treatment outcomes. Also, the poor drug absorption and lack of proper knowledge of the pharmacokinetics of INH had made the rise of INH-resistant mycobacteria inevitable. The conjugation of INH on MC-IONPs is facilitated by electrostatic interaction. The successful conjugation was analyzed using FTIR (Fourier transform infrared spectroscopy) and zeta/DLS (dynamic light scattering). The nanoconjugate exhibited MIC (minimum inhibitory concentration) at 1.5 μg mL^{-1} and MBC (minimum bactericidal concentration) at 3.12 μg mL^{-1}. The nanoconjugate was stable for up to 72 h and showed significant inhibition of replicating bacteria in growth kinetics assay. An increase in ROS (reactive oxygen species) formation is noted in cells treated with the INH–MC-IONP nanoconjugate. In the biofilm model, the mycobacterial biofilm is significantly inhibited (96%) at 12.25 μg mL^{-1} concentration. This nanoconjugate is also effective against persistent mycobacteria. Given these prevailing scenarios the data obtained suggest that this hybrid nanoplatform acts as a promising tool for application in enhancing the effects of INH with lower doses possible.

Received 11th November 2024,
Accepted 27th June 2025

DOI: 10.1039/d4ma01121j

rsc.li/materials-advances

New concepts

A programmable nanoplatform consisting of isoniazid coated on citrate anion grafted multicore magnetic nanoparticles for application in target-based therapy for mycobacterial infection treatment has been developed. The novel structures of magnetic particles obtained by the modified polyol method present clustered morphology with grains as small as 8 nm. By utilizing subsequent electrostatic colloidal sorting to fractionate the suspension of iron salts and thereby sorting their magnetic properties these multicore nanoparticles consisting of maghemite and hematite cores were obtained. Notably, our approach consists of the following: (i) the single core size was about 8–10 nm, which cooperated magnetically to form multicore nanoparticles of size about 30–50 nm. (ii) The cooperative magnetic behavior within highly crystalline multicore magnetic particles subsequently improves therapeutics and diagnostics effectiveness over existing nanostructures when conjugated with a generalized drug. (iii) The mycobacterial targeting efficacy of our strategy impacts the replicating, biofilm, persistent, and dormancy phases of mycobacterium species. Thus, our finding provides new insights into using novel engineered nanoplatforms to treat TB.

1. Introduction

The challenge of fabricating effective therapeutics that are safe for healthy tissues and possess broad-spectrum antibacterial activity lies at the heart of developing antimicrobial resistance-fighting strategies. Finding a single particle system with such a paradoxical feature is hard. Despite years of research, antimicrobial resistance (AMR) continues to be a major worldwide problem. About 170 000 deaths have been attributed to multidrug-resistant (MDR) strains of *Mycobacterium tuberculosis* (TB), while 1.3 million deaths have been attributed to TB infections.[1] Additionally, 10% of tuberculosis cases are currently caused by the extensively drug-resistant (XRD) strain, which has been documented in 92 countries.[2] One essential first-line anti-TB medication that is used in both the intensive

[a] *Center for Biotechnology, Siksha 'O' Anusandhan (Deemed to be University), Bhubaneswar-751003, Odisha, India. E-mail: marakha@soa.ac.in, manoranjan.arakha@gmail.com*
[b] *Indian Institute of Technology Hyderabad, Hyderabad, India*
[c] *Indian Institute of Science Education and Research, Bhopal-462066, India*
[d] *Medical Research Laboratory, IMS & SUM Hospital, Siksha 'O' Anusandhan University, Bhubaneswar, Odisha, India*

and continuation stages of treatment is isoniazid (INH).[3] Currently, TB is targeted by employing combinatorial therapeutics comprising the ''first-line'' anti-TB medications such as ethambutol (EMB), rifampicin (RIF), isoniazid (INH), and pyrazinamide (PZA) for six months (short-term treatment).[4] The distinction between TB patients' and healthy individuals' pharmacokinetic (PK) characteristics is yet to be deciphered. Furthermore, the oral administration of INH makes its absorption less effective for patients with diabetes, HIV, and gastrointestinal disorders.[4] However, the side effects, such as peripheral neurotoxicity, liver toxicity, and renal toxicity, arising from the existing treatment regimens that are being followed also have an impact on patient life quality and adherence to the treatment strategies.[4] In addition, over the past ten years, the number of TB drug-resistant cases has increased dramatically. 82% of cases of multidrug resistance, which is problematic, exhibit resistance to both RIF and INH.[5] Despite the widespread use of these ''first-line'' drugs, specifically INH, the optimal dose of its treatment is yet to be established. Consequently, this leads to treatment failure and an increase in multi-drug resistance of TB strains. As a result, the need for an effective TB treatment regime is the need of the hour.

The concept of a nanoparticle-mediated drug delivery approach holds great promise in treatment and diagnosis; however, the precision needs are still unmet. Conjugating the active molecules with biocompatible polymeric carriers such as functionalized poly(ethylene glycols) or their block copolymers allows for effective drug administration and ensures sustained activity and controlled drug release.[6] Recently, magnetic micro- and nanoparticles have found growing utility in biomedical applications, such as in magnetic separation, magnetic resonance imaging (MRI), and targeted drug administration.[7] These applications leverage the principle of local application of a magnetic field to achieve targeted action of medical drugs, ensuring the delivery of active substances directly to the afflicted tissue. This approach is especially relevant for cytostatic agents like doxorubicin.[8] We have utilized this approach in a novel engineered nanoparticle consisting of multiple cores. In medicinal applications, the hydrodynamic size of nanoparticles is crucial as it affects their circulation half-life in the body. Particles smaller than 10 nm are quickly excreted *via* renal clearance, while those larger than 200 nm are taken up by phagocytes and concentrated in the spleen.[9] Both extremes result in a rapid decrease in blood serum concentration. Therefore, particles within 10–200 nm range are optimal for prolonged circulation. Particles smaller than 2 nm are generally unsuitable for medicinal use due to potential toxicity from intracellular organelle damage.[8,9] Also, the attachment of multiple cargos to the nanoparticle surface introduces complexity, high production costs, and extensive purification procedures along with low yield, thereby significantly affecting its scalability and efficiency.[10] Therefore, new paradigms in drug discovery are widely being explored to address the need for novel antibiotics.

Given all these considerations in this work, we provide a conceptual advance in the field. Accordingly, we have utilized a one-pot polyol approach and subsequent colloidal sorting to fractionate the suspension of ferrous and ferric salts by their size and magnetic properties. Citrate anions have been used to stabilize the nanostructure of the magnetically multicore nanoparticles. The three-dimensional orientation of primary cores results in enhanced magnetic susceptibility, allowing them to be used in precision medicine and therapeutics. This highly crystalline superparamagnetic multi-core iron oxide nanoparticle grafted with citrate anions has been loaded with the first-line TB antibiotic isoniazid (INH). In particular, we demonstrated that the conjugation has prompted specificity and enhanced antimycobacterial propensity against *Mycobacterium smegmatis.*

2. Experimental details

2.1. Materials

Iron(III) nitrate nonahydrate ($Fe(NO_3)_3 \cdot 9H_2O$, 98%), sodium hydroxide (NaOH, 99.99%), diethylene glycol (DEG, 99%), sodium citrate tribasic dihydrate (98%), *N*-methyl-diethanolamine (NMDEA, 99%), nitric acid (HNO_3, 70%), iron(II) chloride tetrahydrate ($FeCl_2 \cdot 4H_2O$, 99%), ethyl acetate, acetone, ethanol, and iron(III) chloride hexahydrate ($FeCl_3 \cdot 6H_2O$, 99%) were purchased from SRL chemicals, India Pvt. Ltd.

2.2. Synthesis of multicore iron oxide nanoparticles (MC-IONPs)

The synthesis of MC-IONPs was carried out according to the protocol outlined by Hugounenq *et al.*, with slight modifications.[11] 40 mL of DEG and 40 mL of NMDEA (1 : 1 (v/v) ratio) were mixed to dissolve $FeCl_3 \cdot 6H_2O$ and $FeCl_2 \cdot 4H_2O$ in a 4 : 2 ratio. For 1 h, the mixture was stirred. Subsequently, 0.64 g (16 mmol) of NaOH was dissolved in a 40 mL mixture of DEG and NMDEA (1 : 1 (v/v) ratio). The iron chloride solution was added, and the mixture was stirred for another three hours. Next, the temperature was raised to 220 °C. Following the adjustment of the temperature to 220 °C, the solution was stirred for 18 hours and then cooled slowly to room temperature by removing the heating plate. The black sediments were magnetically separated and repeatedly cleaned with a 1 : 1 (v/v) solution of ethanol and ethyl acetate to remove organic and inorganic contaminants. Ten percent nitric acid treatment was used to get rid of any potential iron hydroxides. To prepare 10% nitric acid, 72.5 mL of the 69% nitric acid solution was added to 27.5 mL of deionized water to make 100 mL of 10% nitric acid solution. Then, after dissolving 8.25 g of the sample of iron(III) nitrate in 20 mL of water, the solution was added to the nanoparticles. The mixture was then heated to 80 °C for 45 minutes to fully oxidize the nanoparticles. Following, a further 10% nitric acid treatment, the particles underwent two rounds of acetone and diethyl ether washing before being re-dispersed in water. Currently, maghemite nanoparticles in an aqueous dispersion are stable in basic or acidic environments.

Citrate anions were grafted onto their surface by adding 1 g of citric acid per 20 mL of iron oxide nanoparticles to increase

colloidal stability at biological pH. The nanoparticles were magnetically extracted from the excess citrate and washed using deionized water. The particles were dried at 60 degrees.

2.3. Preparation of isoniazid (INH) loaded multicore iron oxide nanoparticles (INH–MC-IONPs)

For loading of INH on MC-IONPs, a facile electrostatic assembly approach was followed. Precisely, 1 mg mL^{-1} aqueous INH stock was prepared. The INH solution was separately mixed with MC-IONPs (2 mg mL^{-1}) and continuously stirred at 120 rpm at room temperature for 18 hours to facilitate INH adsorption upon MC-IONPs. The resulting isoniazid multicore nanoparticle (INH–MC-IONP) nanoconjugates were then centrifuged and washed twice to remove the unbound drug moieties and lyophilized to be used for further analysis. The ratio of MC-IONPs to INH was 2 : 1.

2.4. Characterization of the nanocomposite

Powder X-ray diffraction (XRD) (Rigaku Miniflex 600, Japan) was used to determine the structure, crystallinity, and various phases of the MC-IONPs. With a step size of 0.02° [2θ] and a scan rate of 3° per minute, the monochromatic X-ray beam was generated from Cu-Kα radiation with λ = 1.5406 Å. The data were acquired in the 2θ range of 20°–80°. A 40 kV voltage and a 20 mA current were used to analyse the samples. Employing PAN Analytical X'Pert HighScore software, the acquired data were further examined. The bond level features were revealed by the IR spectra, which were collected on a PerkinElmer (US) FTIR spectrophotometer within the 4000–400 cm^{-1} range. The produced nanocomposite was directly evaluated for size, size distribution, and colloidal stability using a zeta potential analyzer (Zeecom Instrument). The dielectric constant for the experiment was 78.26. The cell thickness and width were 0.205 mm and 10.00 mm, respectively, with an SL (front) of 0.043 mm and SL (back) of 0.162 nm. The electrode distance was 3.60 cm. The voltage at which the zeta potential experiment was conducted was set at 110 V. The hydrodynamic sizes of the fabricated nanomaterials were measured by dynamic light scattering (DLS) with a laser wavelength of 632.8 nm, and a scattering angle of 90°, and the refractive index of the dispersant medium was 1.33. For the zeta potential analysis and DLS analysis, the nanoconjugates were uniformly dispersed in phosphate buffer (pH 7.4) and sonicated for 20 minutes before characterization. Using an FE-SEM (JEOL), the morphological characteristics of the prepared nanocomposites were examined after the gold coating for 3 minutes. A JEM-2100F electron microscope, fitted with a 4k × 4k Gatan CCD camera and a high-resolution pole piece, was used for transmission electron microscopy (TEM) investigations. The electron microscope was operated at 200 kV. The TEM images have been used to calculate the nanoflowers' diameter using the ImageJ program.

2.5. Antimicrobial activity of the nanoconjugates

2.5.1. Bacterial strains and reagents used in this investigation. *M. smegmatis* (MTCC 14468), a non-tubercular bacterium, was purchased from MTCC Chandigarh for this study. *M. smegmatis* was grown at 37 °C for 48 h in a shaker incubator using Middlebrook's 7H9 broth medium with 10% growth supplement OADC, 0.05% Tween 80, and 0.2% glycerol. Bacilli were then maintained on 7H11 agar media and stored at 4 °C for further use.

2.5.2. Chemicals required. Isoniazid (I3377-5G), glutaraldehyde solution (Cat. No. 111-30-8), osmium tetroxide (75632-5mL), and menadione (M5625-25G) were purchased from Sigma Aldrich, India. Reagents like 7H9 (M198-500G), 7H11 (M511-500G), OADC (FD018-50mL), and crystal violet (Cat. No. TC510-25G) were purchased from HI media. XTT (X6493-100mG) and Alamar blue dye (DAL1100-100mL) were purchased from Thermo Fisher Scientific. 2′,7′-Dichlorodihydrofluorescein diacetate (DCFH-DA) (85155-100mG) was purchased from Cayman chemicals.

2.5.3. Assessment of anti-mycobacterial activity

MIC and MBC determination. M. smegmatis bacilli were cultured to the log phase, characterized by an optical density of 0.6–0.8 at 600 nm, and then inoculated at a concentration of 10^5 bacteria per well into a 96-well plate containing serial dilutions of isoniazid, MC-IONPs, and the INH–MC-IONP nanocomposite. The plates were subsequently incubated at 37 °C for 48 h. To determine the minimum inhibitory concentration (MIC), each well was supplemented with 1× Alamar blue (Invitrogen), and the colour change from blue to pink was observed after 1 h of incubation for *M. smegmatis*. Positive controls consisted of wells containing only media and bacteria, while negative controls contained only media. For assessing the minimum bactericidal concentration (MBC) of *M. smegmatis*, dilutions from each well were plated onto 7H11 agar plates and then incubated for 48 h at 37 °C. The MIC and MBC tests were conducted in triplicate, and the results were interpreted as the same values.

After the evaluation of MIC, a growth kinetic study of isoniazid, MC-IONPs, and the INH–MC-IONP nanocomposite at MIC doses was executed against *M. smegmatis*. The bacteria were cultivated in a 7H9 medium supplemented with OADC (oleic acid, albumin, dextrose, and catalase) until reaching a final optical density of 0.05. A control group was established with no treatment to serve as a baseline for growth comparison. Incubation was conducted at 37 °C, and the optical density (OD) was assessed at 600 nm at 24-hour intervals over 72 h.

ROS generation activity of isoniazid, MC-IONPs and INH–MC-IONPs against M. smegmatis. The quantification of reactive oxygen species (ROS) generated by isoniazid, MC-IONPs, and the INH–MC-IONP nanocomposite was assessed using 2′,7′-dichloro-dihydro-fluorescein diacetate (DCFH-DA). *M. smegmatis* was cultured in 7H9 medium supplemented with 10% OADC. MC-IONPs and INH–MC-IONP nanocomposites were administered at a minimum inhibitory concentration (MIC) with 10^5 cells per well. Following a 24 and 48-h incubation period, 5 μL of 10 mM DCFH-DA was introduced into each well, and fluorescence intensity was measured at an excitation wavelength of 503 nm and an emission wavelength of 523 nm. Fluorescence intensity was observed at every 24-hour

interval for 48 h. Positive controls consisted of wells containing bacteria in 7H9 broth, while negative controls contained only media.

Antibiofilm activity of isoniazid and INH–MC-IONPs. M. smegmatis was cultured for 48 h until reaching an optical density of 0.7–1.0 at 600 nm. Biofilm formation was induced using Sauton's media in a 96-well plate and incubated for 4–5 days. Isoniazid (50 μg mL^{-1}), MC-IONPs (50 μg mL^{-1}), and the INH–MC-IONP nanocomposite (50 μg mL^{-1}) were applied. The biomass was assessed using crystal violet (1%) following phenotypic observation. After Sauton's medium was removed, crystal violet was added to each well and allowed to incubate for 1 h. The biofilm was then rinsed 2–3 times with PBS (pH 7.4). Subsequently, 95% alcohol was introduced into each well and incubated for 15 minutes before absorbance readings were taken at 592 nm.

Cell viability was determined using the XTT-menadione-reducing assay. After washing the biofilm with phosphate-buffered saline (PBS), a freshly prepared solution containing XTT (200 μM, 48 μL) and menadione (60 μM, 2 μL) were added to each well, along with 158 μL of PBS. Following a 3 h incubation period, absorbance measurements were recorded at 492 nm using an ELISA plate reader.

Scanning electron microscopy of the M. smegmatis biofilm. Scanning electron microscopy (SEM) was utilized to examine the biofilm formation of *M. smegmatis* with sub-minimum biofilm inhibitory concentration (MBIC). The biofilms underwent a series of procedures for SEM analysis. Initially, sterile Sauton's medium was introduced into a 12-well plate containing sterile coverslips along with a bacterial inoculum comprising a 1 : 100 dilution of bacterial cells per well, treated with sub-MBIC doses of isoniazid, MC-IONPs, and the INH–MC-IONP nanocomposite. This setup was then incubated for 56 hours to facilitate biofilm establishment. Following the phenotypic observation, the biofilm-covered coverslips were retrieved and rinsed with distilled water and 1× PBS. Subsequently, 2.5% glutaraldehyde solution was added to the coverslips, followed by 20-minute incubation at 4 °C to fix the adherent biofilms. After cleaning the coverslips with distilled water and 1× PBS, they were stained again for one hour at 4 °C using 1% osmium tetroxide. The coverslips were then washed with distilled water and 1× PBS, dried with varying concentrations of ethanol (30%, 50%, 70%, 90%, and 100%), and air dried at room temperature. The slides were incubated overnight at 4 °C before undergoing SEM imaging.

Persistent assay. Log phase *M. smegmatis* was diluted to an A_{600} of 0.05 and then treated with 50 μg of isoniazid and a series of concentrations of the INH–MC-IONP nanocomposite for 48 h of incubation. After incubation, the CFU was determined with dilutions of samples for persistent assay on 7H11 agar.

Nutrient starvation model for M. smegmatis. Log phases of *M. smegmatis* cultures were subjected to centrifugation and were washed with 1× PBS. The supernatant was discarded and the pellet was dissolved in 1× PBS with Tween-80, and the volume was made up accordingly. The bacteria were allowed to incubate at 37 °C for 15 days. To verify vitality, they were plated on 7H11 agar plates after incubation. Dormant bacteria were treated with isoniazid (50 μg mL^{-1}), MC-IONPs (50 μg mL^{-1}), and the INH–MC-IONP nanocomposite (50 μg mL^{-1}) and adjusted to OD 0.1 to determine MIC in a 96 well plate. The plate was incubated for 48 h and then 1× Alamar blue was added to each well to determine to the MIC. Inoculum from each well was plated on 7H11 agar to determine the MBC.

Cytotoxicity assay. To check the cytotoxic effect of the nanoparticles by the colorimetric technique, the HEK-293 cell line was used. The cells were cultured in DMEM media supplemented with 7.5% FBS and 1% Penstrep. The cells were seeded in a 96-well plate (5000 cells per well) until they became 80–90% confluent. For the MTT assay, HEK-293 cells were seeded in a 96-well plate at 5×10^3 cells per well in 200 μL DMEM media and cultured to confluence over 1 day at 37 °C and 5% CO_2. The cells were exposed to different concentrations of the nanoparticle treatment (0.7 μg mL^{-1} and 1 mg mL^{-1}) for 24 h. After 24 h of treatment, 0.5 mg mL^{-1} concentration of MTT solution was prepared in 1× PBS and 100 μL of the solution was added to each well. Then the 96-well plate was incubated for 3 hours. The MTT solution was removed after 3 h and 100 μL of dimethyl sulfoxide was added to stop the formazan formation process. The 96 well plate was kept in a shaker under dark conditions for 15 minutes and then the absorbance was measured at 570 nm.

Statistical analysis. The triplicate data obtained from the experiments conducted for growth kinetics assay, ROS assay, XTT/biofilm assays, and cytotoxicity assays were analysed using Minitab statistical software for Windows. To determine the significance, a one-way analysis of variance (ANOVA) was conducted, followed by Dunnett's *post hoc* test. A *p*-value of ≤ 0.05 was considered to indicate significance. The results were presented as the mean ± standard deviation (SD)/standard error of the mean (SEM) of three biological experiments for each treatment, with three appropriate replicates conducted under similar conditions, unless otherwise specified.

3. Results and discussion

3.1. Characterization of MC-IONPs

An efficient method for synthesizing metal oxide nanoparticles with tunable size and shape is the polyol approach. The temperature, precursor, solvents, and reaction time can all be modified to adjust the parameters. The method leverages the solvothermal synthesis approach involving polyols (NMDEA + DEG) as solvents and reducing agents (NaOH) under controlled heat to facilitate the formation of iron oxide nanoparticles. In our experiment, we have carried out the alkaline hydrolysis of $FeCl_3 \cdot 6H_2O$ and $FeCl_2 \cdot 4H_2O$ in a stoichiometric ratio within a 1 : 1 w/w polyol mixture that contains DEG and NMDEA at

220 °C for over 12 h. It was found that the collected particles had come together to form a structure resembling a flower. Therefore, some literature also mentions them as ''nanoflowers''. Previous research has demonstrated that clustering and coalescence are due to the heating ramp and high-temperature phase.[11] Following the development of the nanoparticles, forced oxidation using an iron nitrate solution was used to oxidize them into maghemite to maintain their chemical stability. As a result, monodisperse multicore nanoparticles (MC-IONPs) with a mean diameter of around 11.0 nm were obtained. The probable series of reactions leading to the formation can be summarised as follows:

Dissolution of ferric salts in polyols (DEG + NMDEA) is followed by their complexation and initial stabilization.

$$FeCl_3{\cdot}4H_2O \rightarrow Fe^{3+} + 3Cl^- + 4H_2O \quad (1)$$

$$FeCl_2{\cdot}6H_2O \rightarrow Fe^{2+} + 2Cl^- + 6H_2O \quad (2)$$

Following the addition of NaOH, the formation of iron hydroxides takes place

$$Fe^{3+} + 3OH^- \rightarrow Fe(OH)_3 \quad (3)$$

$$Fe^{2+} + 2OH^- \rightarrow Fe(OH)_2 \quad (4)$$

Upon heating, growth and nucleation take place leading to the formation of IONPs

$$3Fe(OH)_2 \rightarrow Fe_3O_4 + 2H_2O + H_2 \quad (5)$$

The nanoparticles were arranged in three dimensions, as seen by TEM microscopy, Fig. 1(a). The MC-IONPs are made up of a collection of combined cores that have the same facet (Fig. 1(b)). The distance between the lattice planes is indicated in Fig. 1(c), which is around 0.193 nm. The nanoflowers are isotropic assemblages of cores that create almost spherical porous super-crystals; the total diameter depends on the number of cores present, according to the results of electron tomography. Fig. 1(d) shows the selected area electron diffraction (SAED) pattern as recorded from the area containing a high number of nanoparticles. The rings in the image can be indexed as (220), (311), (400), (422), (511), and (440), which are reflections of cubic magnetite in agreement with XRD results.[12]

SEM microscopy revealed the morphological feature of MC-IONPs, Fig. 1(e). They appear to be like spherical nanoparticles. EDAX analysis revealed the elemental composition of the MC-IONPs with 82.2% of iron and 17.8% of oxygen being detected (Fig. 1(f)). The inset in Fig. 1(g) presents the elemental analysis of MC-IONPs with yellow representing oxygen and blue representing iron.

Following the structural investigations by TEM, XRD patterns are also investigated and found to be consistent showing the γ-Fe_2O_3 crystalline structure as shown in Fig. 2(a). The peak positions obtained at (220), (311), (400), (422), (511), and (440) correspond to 2θ values of 30.06, 35.41, 43.03, 56.91, and 62.49 degrees respectively.[12] The mean crystallite diameter (d_{XRD}) for the single-core nanoparticles was calculated using the Scherrer equation and found to be 9.2 nm, which was in good agreement with a d_{TEM} value of 10.3 nm obtained from the TEM image. Nevertheless, the d_{XRD} ranged from 9.2 to 15.6 nm for the multicore nanoparticles, which is consistently smaller than the TEM size. The high-resolution imaging revealed minor crystal structural misalignments at the core interface, which could account for the difference in the XRD and TEM readings.

The bond level properties of the formulated MC-IONPs were identified by FTIR analysis as shown in Fig. 2(b). The band found at 2870 cm^{-1} is attributed to the stretching of the C–H bond.[13] The band found at 1600 cm^{-1} is attributed to bending vibrations of H–N–N.[13] One explanation for the band seen at 1247 cm^{-1} and 1065 cm^{-1} is C–C stretching. The spectrum peak obtained at 1388 cm^{-1} corresponds to C–H methyl rock and is typically the IR spectrum of octane. Since there has been use of organic compounds during the synthesis these C–H vibrations are noted. The bands around 2360 cm^{-1} are extremely sharp. These bands around 2360 cm^{-1} are from the carbon dioxide gas. The metal–oxygen interaction is represented by the band seen at 534 cm^{-1}.[14]

MC-IONPs' negative charge was demonstrated by their negative zeta potential value as shown in Fig. 2(c). The fact that the particles have a high negative zeta potential of −35.4 mV indicates that they are stable.[15] The average hydrodynamic size corresponds to around 322.9 nm.[15] DLS analysis showed that multi-core nanoparticles dispersed in the colloidal solution (Fig. 2(d)). The colloidal stability of the suspension at room temperature can also show the collective behavior of the intraparticle systems.[15,16] The magnetic characteristics are revealed by the intraparticle interactions.[17] The colloidal stability is largely attributed to the lack of intraparticle magnetic interactions, indicating that the superparamagnetic characteristics of MC-IONPs are retained. Furthermore, a larger apparent magnetic size and decreased anisotropy imply that our multicore nanomaterials exhibit increased magnetic properties rather than the magnetic behavior of the individual cores.

The combined cores rotate to share the same crystallographic orientation and then undergo surface energy minimization during the polyol synthesis of the MC-IONPs. Consequently, the FCC structure of nano-formulation is a mono-crystalline inverse spinel. Recently, it has been demonstrated that the unique structure of multicore iron oxide nanoparticles is responsible for their exceptional performance as an MRI contrast agent and as a heating mediator for magnetic hyperthermia. The cooperative behavior of multicore particles can be attributed to exchange interactions between their constituent cores, as demonstrated by a comparison of their magnetic characteristics with those of single cores.[18] The crystal continuity at the core interface, which also guaranteed spin orientation continuity, made the collective magnetic behavior of internal cores possible.[18] Thus, the multicore particles showed increased sensitivity in comparison to the single core, while maintaining a superparamagnetic behavior due to a reduced surface anisotropy.[19] Their exceptional MRI relaxivity and heating power were caused by the combination of their low magnetic, high saturation magnetization, and high sensitivity.

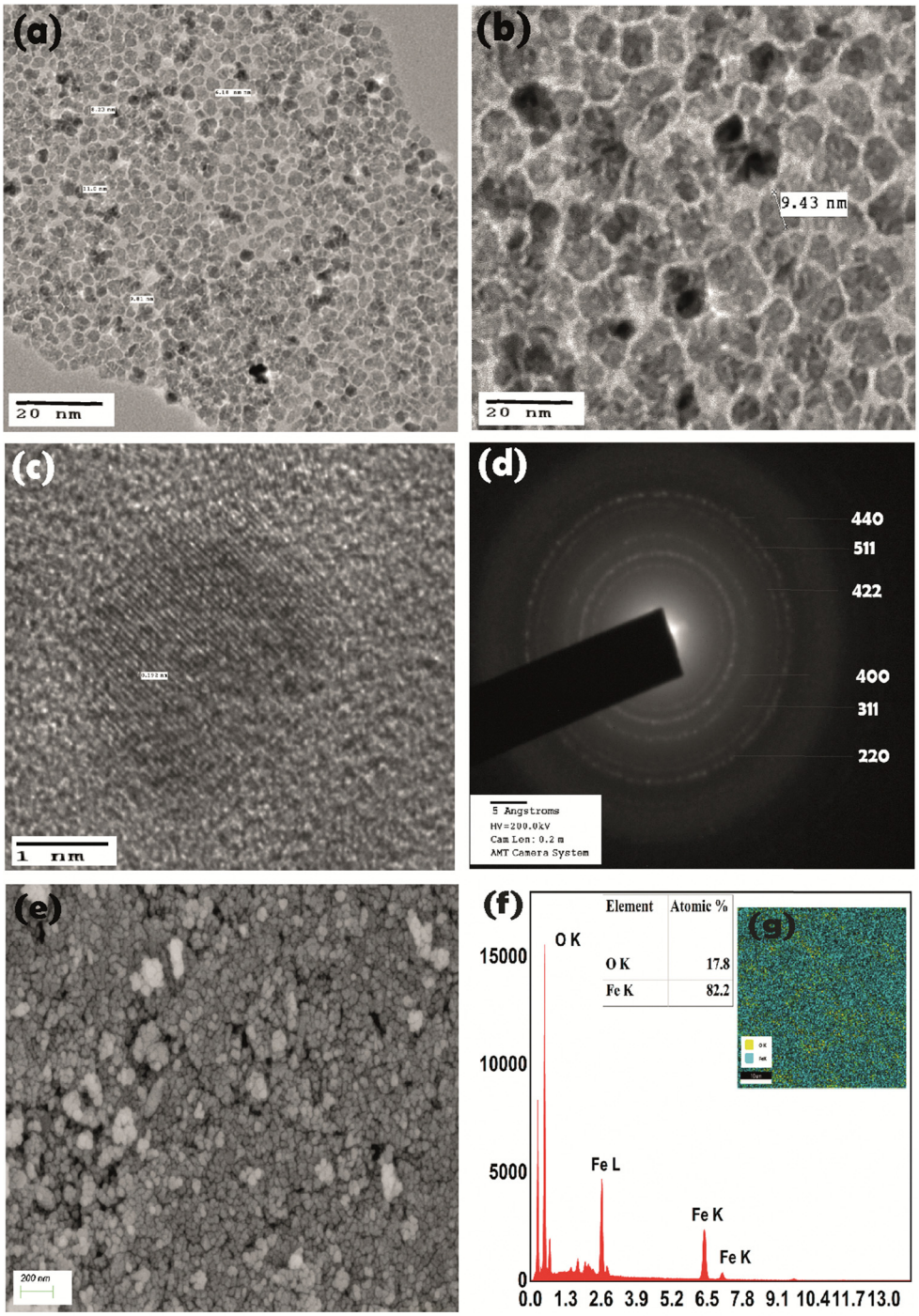

Fig. 1 SEM and TEM images of MC-IONPs. (a) TEM image of MC-IONPs taken at a 20 nm scale. The size of individual clusters ranges below 10 nm. The clusters are morphologically distinguished. (b) TEM image highlighting multiple cores fused. (c) Electron fingerprint image as obtained by TEM. (d) SAED pattern of MC-IONPs. (e) SEM image of MC-IONPs. (f) EDAX analysis of MC-IONPs and elemental analysis of the obtained particles (inset (g)).

Therefore, the biocompatible, water-dispersed multicore particles made of pure iron oxide hold great promise for biomedical applications involving the colloidal chemical synthesis of core–shell nanocomposites. This is because it presents a unique opportunity to control the degradability of MC-IONPs, allowing them to retain their magnetic properties during treatment and break down over time to be either eliminated by biliary excretion or processed locally by iron metabolism.[20] The notion of hybrid nanostructures, comprising materials with varying environmental reactivity, presents a novel pathway for regulating the destiny of nanoparticles within organisms. To evaluate this technique *in vivo*, more research is required.

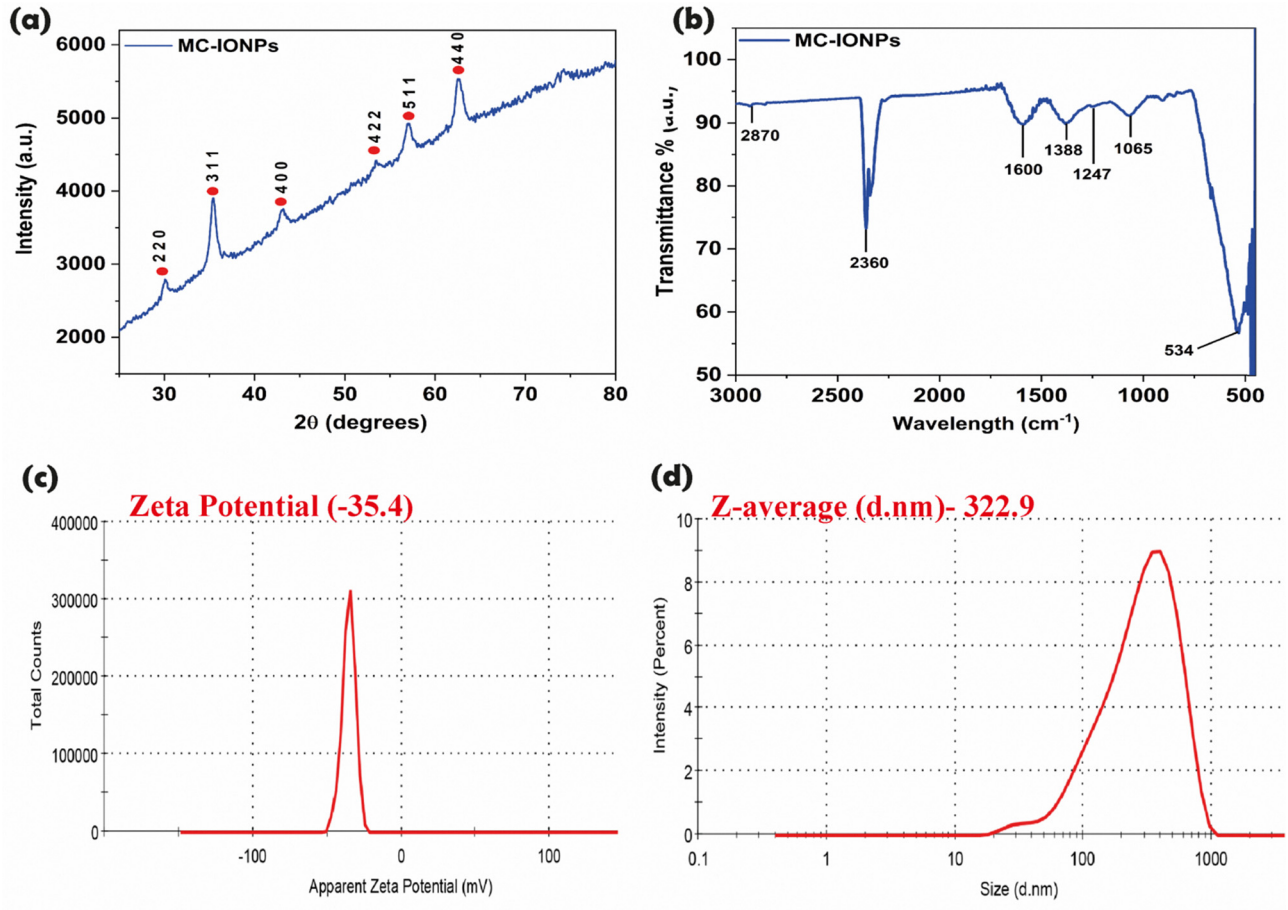

Fig. 2 Analysis of crystallinity, functional group, charge, and size: (a) XRD pattern of MC-IONPs. (b) FTIR bands as obtained for MC-IONPs. (c) and (d) Zeta potential and size analysis by DLS of MC-IONPs.

3.2. Characterization of the nanocomposite

Initially, FTIR spectroscopy was used to confirm that the first-line TB antibiotic, isoniazid, was loaded efficiently onto MC-IONPs (Fig. 3(a)). The existence of C–H stretching vibrations was found in the range of 3100–3000 cm^{-1} for isoniazid due to the presence of heteroaromatic structure for INH.[21] The FTIR band at 3053 cm^{-1} for isoniazid is therefore attributed to stretching vibrations of the C–H bond. The strong bands resulting from C═O stretching vibrations occur in the range of 1870–1560 cm^{-1}.[22] Hence, the C═O stretching mode is responsible for the strong band seen at 1662 cm^{-1} in the FTIR spectrum. Due to NH bending, primary and secondary amides exhibit a band or bands in the range of 1650–1515 cm^{-1}. Amine groups are responsible for the band observed at 1548 cm^{-1}. C–C vibrations are associated with the amine bands at 1412 cm^{-1}.[21] Absorptions in the range of 1260–700 cm^{-1} are observed for the C–C stretching vibrations. As a result, C–C stretching has been identified due to the band seen at 1220 cm^{-1}, 1136 cm^{-1}, 1019 cm^{-1}, 886 cm^{-1}, 850 cm^{-1}, and 660 cm^{-1}.[22] For INH–MC-IONPs the peaks appeared at 3305 cm^{-1}, 2866 cm^{-1}, 2366 cm^{-1}, and 1656 cm^{-1} due to functionalization. The peak at 2866 cm^{-1} corresponds to the C–H stretching vibrations from aliphatic chains. The peaks at 1656 cm^{-1} are usually indicative of C═O stretching from the carbonyl group.[23] The isonicotinoyl hydrazine structure contains a carbonyl group, which could give rise to this peak. Also, this peak is indicative of the INH being conjugated to a nanoparticle surface or matrix.[23] The peak obtained at 516 cm^{-1} is due to metal–oxygen interaction. The zeta potential value of the synthesized INH–MC-IONP nanocomposite was found to be −38.8 mV (Fig. 3(b)). The higher zeta potential might be attributed to the conjugation of negative INH. Accordingly, the hydrodynamic size of the INH–MC-IONP nanocomposites was found to be 359.7 nm. This increase in size upon INH conjugation is attributed to the electrostatic assembly of the drug on the surface of citrate-grafted MC-IONPs (Fig. 3(c)).

3.3. Antimycobacterial activity of INH, MC-IONP and INH–MC-IONP nanoconjugates

Bacterial population and nanoconjugate sensitivity:

M. smegmatis shares a significant amount of genetic similarity with pathogenic mycobacteria like *M. tuberculosis* and *M. leprae*, thereby making them an excellent model for understanding how mycobacteria develop resistance to anti-tuberculosis drugs like isoniazid and rifampicin.[24] Also, the cell wall structure is similar to *M. tuberculosis*, making them

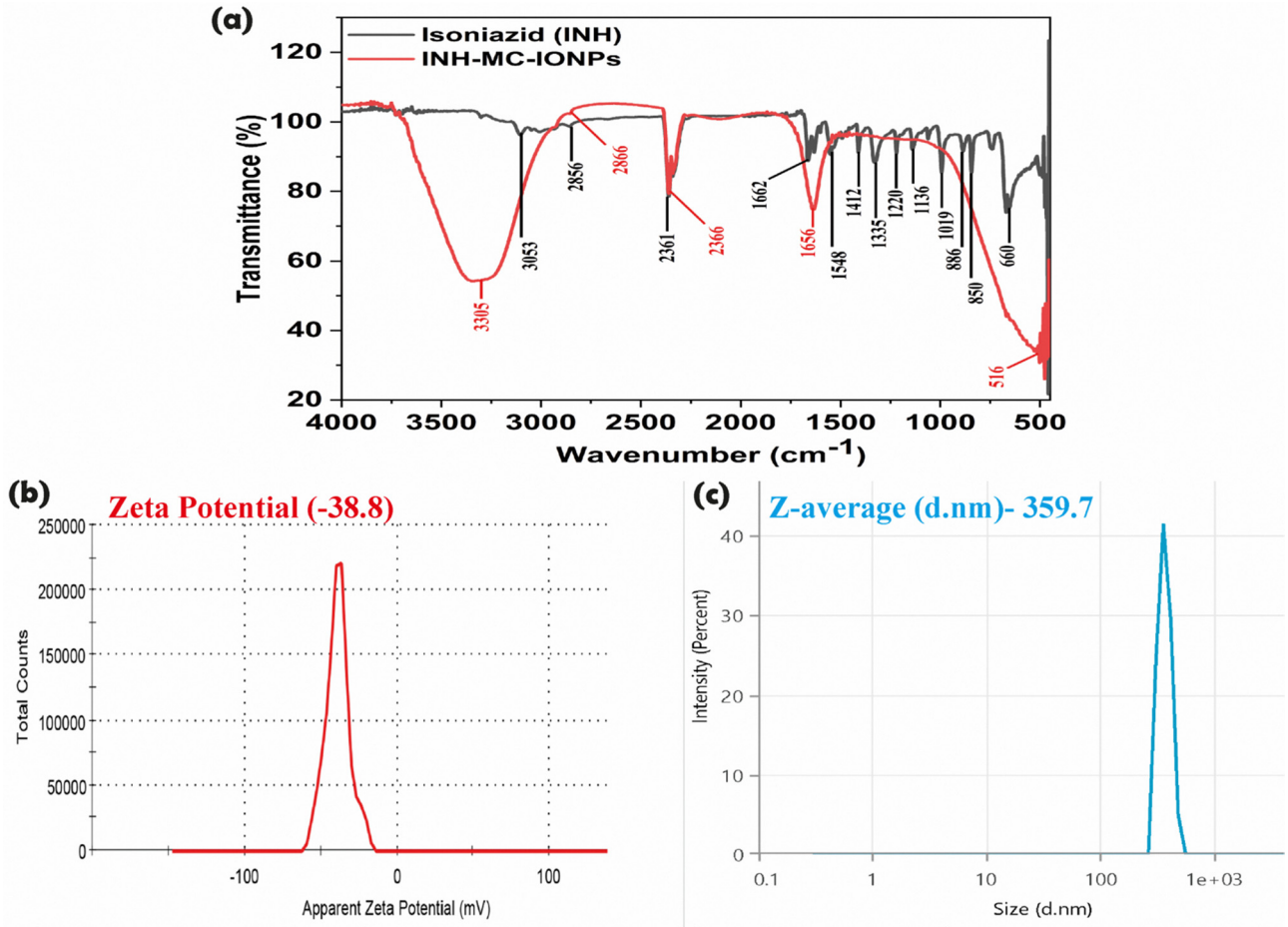

Fig. 3 Confirmation of conjugation of INH on MC-IONPs. (a) FTIR analysis of INH in comparison with INH–MC-IONPs. (b) and (c) zeta potential and DLS analysis of INH–MC-IONPs.

more relevant for the study of the resistant phenomenon.[24] The strain of *M. smegmatis*, when grown in its specific culture medium treated with various concentrations (0.07–250 μg mL^{-1}) of INH, MC-IONPs, and INH–MC-IONP nanoconjugates, showed differential resistance and sensitivity behavior (Table 1 and Fig. 4). Among the test samples, MC-IONPs were found ineffective against the mycobacterium strain even at a concentration of 250 μg mL^{-1}. However, the loss of mycobacterial cell viability was visible at 12.5 μg mL^{-1} and 1.5 μg mL^{-1} for the first-line TB drug INH and INH–MC-IONP nanoconjugates respectively. Positive controls containing only media and bacteria exhibited a clear blue-to-pink shift, confirming bacterial viability. Negative controls, containing only media, remained blue throughout the experiment, verifying the absence of contamination. The cell viability decreased consistently with the increase in concentrations of INH and INH–MC-IONP nanoconjugates and was further completely lost at the MBC dose. The MBC concentrations of INH and INH–MC-IONP are 50 and 3.12 μg mL^{-1} respectively.

Table 1 MIC and MBC of isoniazid (INH), MC-IONPs, and INH–MC-IONP nanoconjugates against *M. smegmatis*

Nanoparticles (μg mL^{-1})	MIC	MBC
MC-IONPs (multicore iron oxide nanoparticles)	250	—
Isoniazid (INH)	12.5	50
INH–MC-IONP nanoconjugates	1.5	3.12

3.4. Measurement of growth and reactive oxygen species release dynamics

For the evaluation of growth under the influence of INH, MC-IONPs, and INH–MC-IONP nanoconjugates the MIC dose was chosen for the treatment (Fig. 5a). Upon analysis, the data revealed that the untreated control group of mycobacteria demonstrated a typical growth curve while the highest concentration (250 μg mL^{-1}) of MC-IONPs also followed the same trend. There was exponential growth between 24 and 48 h and it gradually reached the plateau phase at 72 h. In contrast, INH and INH–MC-IONPs were found to adversely affect the growth of *M. smegmatis* when analyzed for time-dependent changes. However, it was found that in the case of the INH–MC-IONP nanocomposite, the optical density measurements at 600 nm remained relatively constant in comparison to INH, which demonstrated an increase in the OD after 50 h. The probable reason might be attributed to the degradation of INH after a period of 50 h.

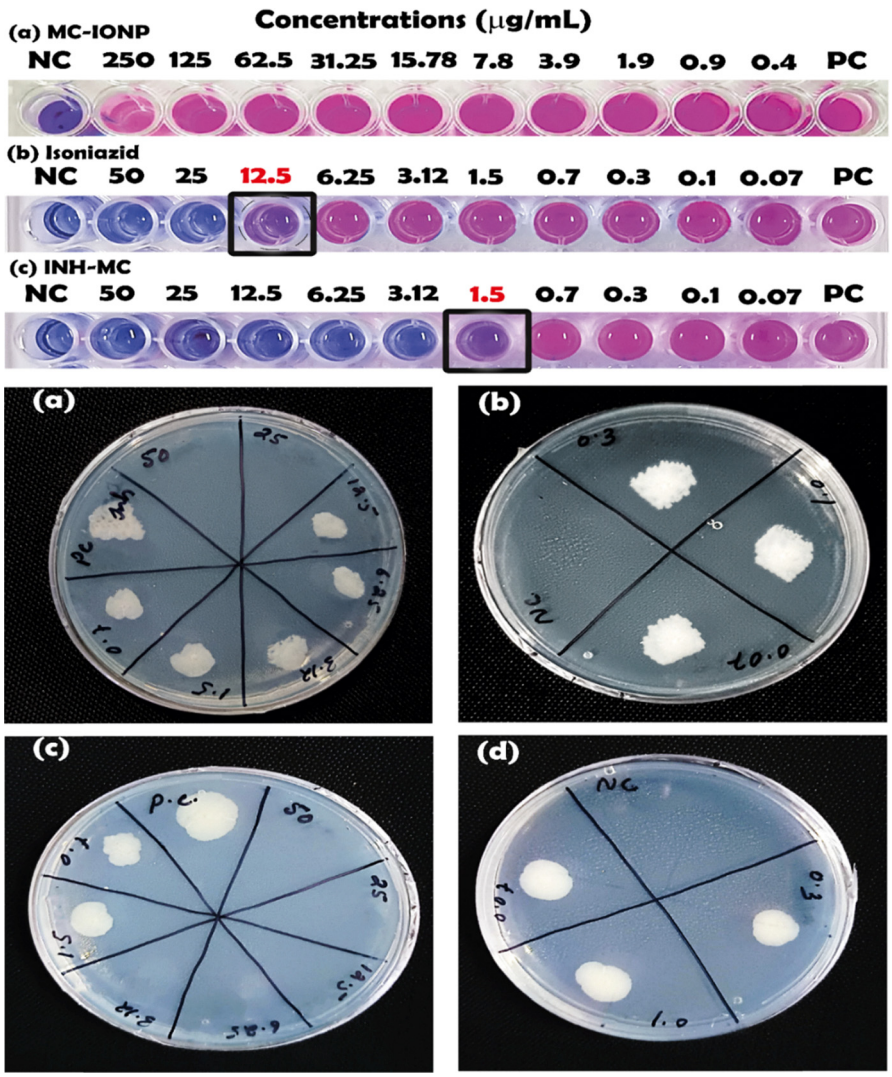

Fig. 4 The figure (a), (b) and (c) in the top panel indicates MIC of MC-IONP, Isoniazid, and INH–MC-IONP respectively against *M. smegmatis*. In the down panel (a), (b), (c) and (d) shows agar plate assay for determining minimum inhibitory concentration (MIC) and minimum bactericidal concentration (MBC) of INH–MC-IONPs against bacterial strains. Zones of inhibition indicate effective antimicrobial activity.

The generation of reactive oxygen species by INH, MC-IONPs, and INH–MC-IONP nanoconjugates was assessed in terms of fluorescence intensity using 2′7-dichloro-dihydro-fluorescein diacetate (DCFH-DA) dye. Fluorescence intensity was measured at 24 h intervals for a 48 h period (Fig. 5(b)). There was a significant increase in the intensity in the INH and INH–MC-IONP treated group compared to the control and MC-IONPs. Overall, the INH–MC-IONP nanoconjugates induced the highest ROS production.

3.5. Assessment of cell viability and biofilm inhibition in biofilm-producing *M. smegmatis*

The antibiofilm activities of isoniazid and the INH–MC-IONP nanocomposite were assessed on *M. smegmatis* biofilms induced in Sauton's media over 4–5 days. Following treatment with each compound (50 μg mL^{-1}), biofilm biomass was quantified using crystal violet staining, and cell viability was determined using the XTT-Menadione-reducing assay. The crystal violet assay revealed a substantial reduction in biofilm biomass in the INH–MC-IONP nanocomposite group compared to the INH (Fig. 6(a) and (b)). The INH–MC-IONP nanocomposite shows approximately 93% of mycobacterial inhibition until a treatment concentration of 3.12 μg mL^{-1} (Fig. 6(c) and (d)), whereas the same concentration of 3.12 μg mL^{-1} of INH shows 55% inhibition of cells approximately. Therefore, the INH–MC-IONP nanocomposite significantly restricts the colonization of bacteria and the formation of biofilm. It can be inferred that the treatment of INH–MC-IONP nanocomposite-induced cell death, thereby restricting the formation of the EPS matrix and disrupting the three-dimensional structure of biofilms. To strengthen this hypothesis, we have also analysed the control and treated mycobacterial groups under a field emission scanning electron microscope (FE-SEM).

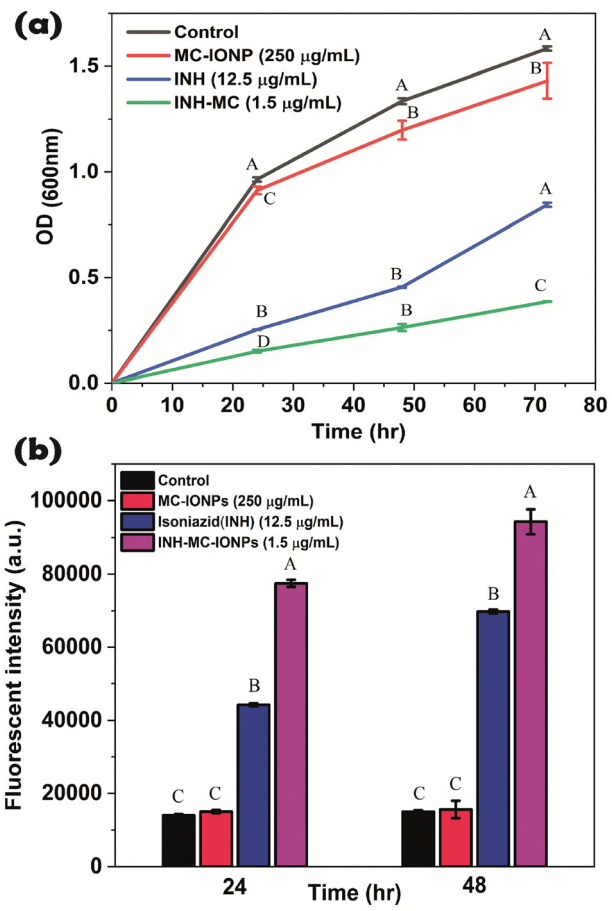

Fig. 5 (a) Growth kinetics of *M. smegmatis* in the presence of MIC doses of isoniazid, MC-IONPs, and the INH–MC nanocomposite over 72 hours. (b) Fluorescence intensity *versus* time graph for the measurement of reactive oxygen species generated following the mycobacterial interaction with the test samples.

Correspondingly, the XTT-menadione assay indicated a marked decrease in cell viability within the biofilms upon treatment. This result is consistent with the biofilm assay with only 7% of viable cells being noted for the INH–MC-IONP nanocomposite and 38% of viable cells being noted for INH.

3.6. Assessment of mycobacterial biofilm morphology under INH and INH–MC-IONP nanoconjugate stress

When examined under a scanning electron microscope, the therapeutic potential of INH and INH–MC-IONP nanoconjugates towards the structural integrity of the mycobacteria varied. Dense fragmented/disorganized cell envelopes were noticed in the case of treated cells. The treated cells' surface displayed a corrugated appearance along with certain depressions and length changes (Fig. 7). For both INH (Fig. 7(c) and (d)) and INH–MC-IONP (Fig. 7(e), (f)), broken and destroyed cells were also seen. The treated cells became far more compacted, which prevented them from proliferating and dividing. Blisters, both single and many, were observed in addition to the irregular cellular architecture. Numerous little bubbles protruded in the cells as a result of the MIC dose (Fig. 7(f).

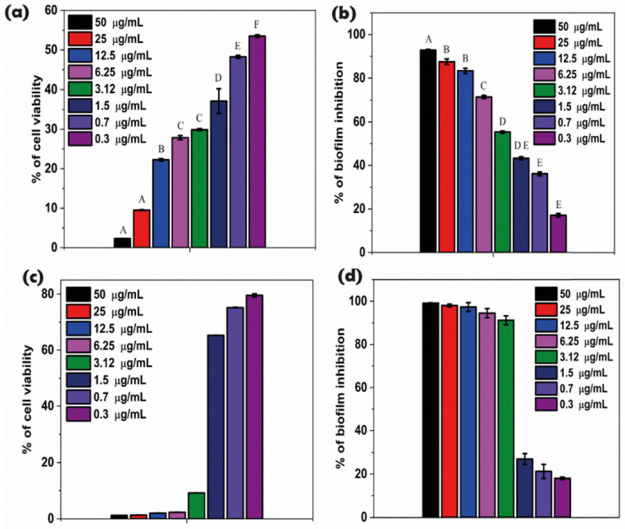

Fig. 6 (a) and (c) XTT-menadione assay of *M. smegmatis* after treatment with isoniazid and the INH–MC-IONP nanocomposite. (b) and (d) Inhibition of *M. smegmatis* biofilms after treatment with isoniazid and the INH–MC-IONP nanocomposite.

Additionally, the exposure to NPs caused multiple dent formations and holes in all four bacterial cell envelopes. The cells were also checked for any presence of nanoparticles by EDAX analysis. Following the results it was found that there is uptake of Fe^{+} ions inside the cells. Thus, this is also supported by the evidence of aberrant morphology and disruption of cell morphology. Dense material and homogeneous biofilms are visible on the surface of the untreated control samples. In contrast, the cells treated with INH and INH–MC-IONP nanoconjugates exhibited a high number of pits, gaps, and dehydrated cells have also been noticed around mycobacteria.

3.7. Effect of INH–MC-IONP nanoconjugates on persistent colonies of *M. smegmatis* bacteria

The persistent assay was conducted to determine the efficacy of treatments against drug-tolerant persistent cells of *M. smegmatis*. Bacteria in the log phase were treated with isoniazid and the INH–MC nanocomposite. CFU enumeration on 7H11 agar plates after 48 hours of incubation revealed a significant reduction in cell count in the INH–MC treated groups compared to isoniazid and untreated control. According to the CFU count (cell count), we can say that INH–MC can inhibit the growth of drug-tolerant persistent bacteria efficiently. As evident the control shows a cell count at 18 166 666.67 ± 251 661.1478, whereas INH treated plates show a decreased cell count at 900 000 ± 264 575.1311. Furthermore, the INH–MC nanoconjugate showed 630 000 ± 615 386.0577 viable cells, thereby establishing the fact that the INH–MC nanoconjugate is effective against persistent *M. smegmatis* (Table 2).

3.8. Effect of INH–MC-IONP nanoconjugates on dormant *M. smegmatis* bacteria

To test the effect of the INH–MC-IONP nanoconjugate against dormant *M. smegmatis* nutrient starvation assay was performed.

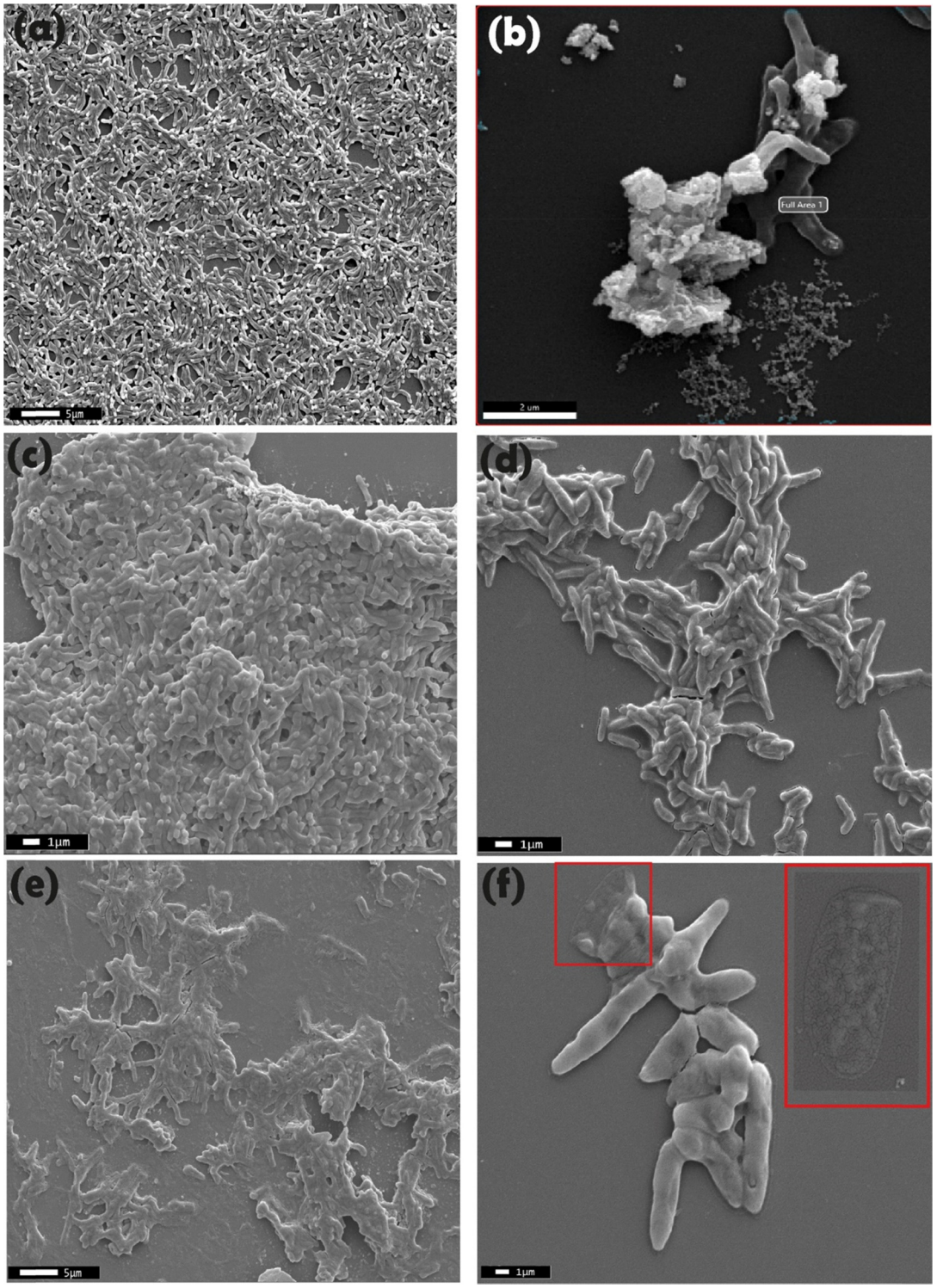

Fig. 7 SEM images of *M. smegmatis* biofilms treated with sub-MBIC doses of isoniazid and the INH–MC nanocomposite. (a) Control (b) uptake of the INH–MC nanoconjugate by *M. smegmatis* as visualized in FE-SEM. (c) 1/4th MIC dose of isoniazid. (d) 1/2nd MIC dose of isoniazid. (e) 1/4th MIC dose of the INH–MC nanoconjugate. (f) 1/2nd MIC dose of the INH–MC nanoconjugate. Inset shows the enlarged image of single bacterial cells, which are killed by the action of the INH–MC nanoconjugate.

Upon addition of 1× Alamar blue and incubation, the results showed that there was no significant inhibition. The INH–MC-IONP nanoconjugate could not generate potential lethality against dormant cells of *M. smegmatis*. The literature states that INH is ineffective against dormant mycobacterial species and this is also true for the INH–MC-IONP nanoconjugate.

It can be inferred that the mechanism behind the action of the INH–MC-IONP nanoconjugate against mycobacteria follows

Table 2 Persistent assay of *M. smegmatis* bacteria

Bacterial strain	Control	INH (50 μg mL^{-1})	INH–MC-IONP nano-conjugate (12.5 μg mL^{-1})
Mycobacterium smegmatis (MTCC 155)	18 166 666.67 ± 251 661.1478	900 000 ± 264 575.1311	630 000 ± 615 386.0577

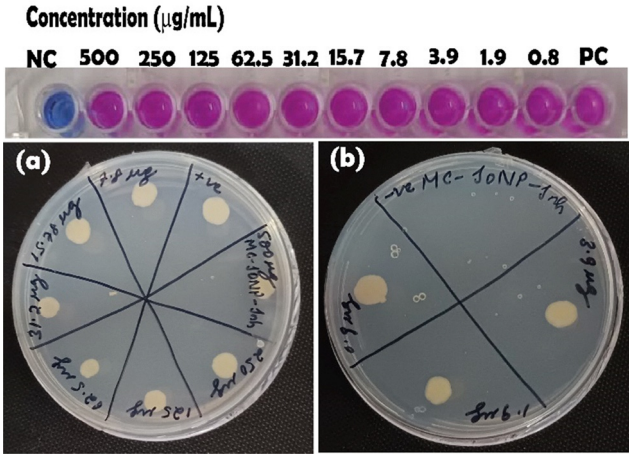

Fig. 8 MIC and MBC ((a) and (b)) of INH–MC-IONPs against dormant *M. smegmatis*.

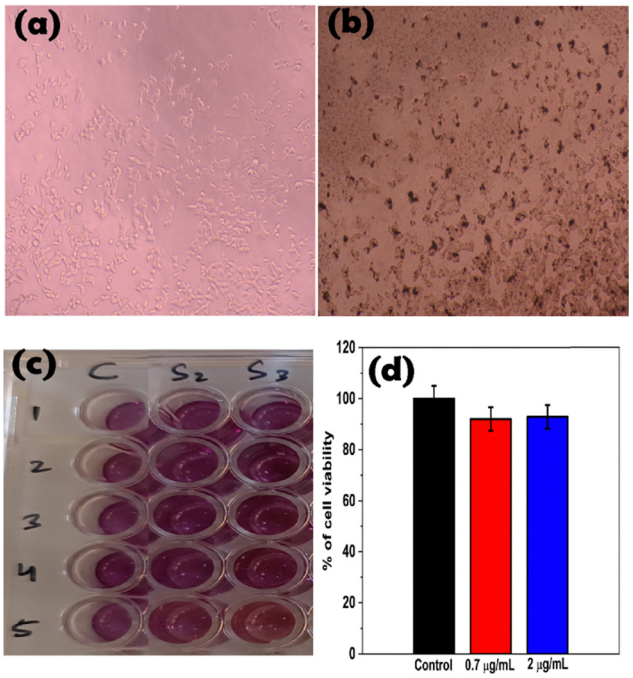

Fig. 9 Cytotoxicity assay of INH–MC-IONP. (a) Control HEK 293 cell lines, (b) INH–MC-IONP treated HEK 293 cell line, (c) cells seeded in 96 well plates, (d) the lowest dose (MIC) and highest dose against HEK 293 cell lines.

the classical mycolic acid inhibition strategy of the INH. Since iron oxide intrinsically does not possess any significant anti-mycobacterial activity it could not aid the pore formation on the bacterial membrane. However, upon internalization, as seen in the persistent model, the INH–MC-IONP nanoconjugates performed superiorly. Also, the loading of lower doses of INH could facilitate lower cytotoxicity when used in *in vivo* models (Fig. 8).

3.9. Cytotoxicity assay of INH–MC-IONPs

Human embryonic kidney (HEK 293) cell lines have been used to test the overall toxicity of INH–MC-IONP nanoconjugates after 24 h of treatment. The lowest concentration tested was the MIC dose *i.e.* 0.7 μg mL^{-1} and the highest dose was 25 mg mL^{-1}. The highest dose was selected according to the maximum concentration of MC-IONPs. Fig. 9(a) presents the normal cell lines without any treatment taken as control. The cells after treatment with INH–MC-IONP nanoconjugates are shown in Fig. 9(b). Due to the presence of iron particles, the cells appear to be brown. The cells were seeded in 96 well plates to be assessed in Fig. 9(c). The results showed that the INH–MC-IONP nanoconjugates have a negligible effect on cell viability even at the highest tested concentrations, Fig. 9(d).

4. Discussion

Substantial success has been attained in the field of nanotheranostics for the use of nanoparticles.[25] However, there are some impediments to nanomedicine becoming an alternative to conventional therapies. The primary reason is the incomplete understanding of the uptake and internalization. Secondly the influence/toxicity and finally the systemic administration and pharmacokinetics.[26] Nanoparticles inside the biological milieu face barriers that limit their efficiency. Moreover, clinical implementation is also hampered by important factors such as scalability, stability, and reproducibility, and finally the high amount of nanoparticle retention in tissues also contributes to the translational gap.[27] Keeping in mind the following things the synthesis of the nanocomposite has been carried out.

The potential mechanism for the development of MC-IONPs is based on the importance of the duration at the final plateau temperature from that of the initial heating period.[11] The heating path produces a variety of multicore sizes; regular heating, or a lower heating slope, better controls seed aggregation. Regular heating hence produces aggregates with a restricted size distribution. Likewise, the initial decrease in seed repulsion causes larger flowers when NaOH is added, and *vice versa*.[11] Aggregate growth is still permitted for the first two hours of the second stage at the plateau temperature. However, further heating at the plateau temperature (220°) mainly induces the coalescence and reorganization of the aggregated seeds.[11] The longer the plateau length, the better aligned the individual seeds' crystal lattices are. Monocrystalline multicores ripen more readily on longer plateaus. The multicores

formed following regular heating display a reduced number of grains (size < 28.5 nm) with high ordering and heating power, which aligns with this method. The fact that the suggested MC-IONPs are made entirely of iron oxide and don't contain any biogenic or potentially harmful inorganic components that can trigger immunogenicity is another important benefit. Furthermore, the chemical and magnetic characteristics of MC-IONPs hold steady over time under both aquatic and growth conditions since maghemite is the fully oxidized form of iron oxide.[28] Their excellent heating properties are further guaranteed by their colloidal stability in culture media, which inhibits the production of large aggregates.[28] This makes MC-IONP-based nanostructures the best option since iron oxide nanoparticles may be broken down and utilized by the body's iron metabolism without causing harm. A magnetic ordering across the interface and, as a result, a cooperative magnetic behavior are favored, as demonstrated by Lartigue *et al.*, by the oriented attachment of individual cores that comprise the IONFs and the ensuing continuity of their crystallographic orientation with a few degree misalignment of the cores.[29] Hence, despite maintaining their superparamagnetic characteristic, the MC-IONPs show increased magnetic susceptibility and decreased surface disorder. Yet, a variety of factors, including the size of the particles' overall mass, the number of cores inside the particles, and their size, affect the magnetic effectiveness of MC-IONPs. Furthermore, studies have already been conducted on the biological effectiveness of citrate-coated multi-core nanoparticles for the treatment of cancer, as well as their interactions with the human breast cancer MCF-7 cell line. Multicore iron oxide nanoparticles were incubated in serum-free media with cells at various iron concentrations (0.2–5 mM). The citrate ligands facilitate the easy adsorption of nanoparticles on the cell plasma membrane, as was previously shown for nanoparticles produced by co-precipitation. This results in quick and effective uptake of the particles by tumor cells by endocytosis. On the other hand, because of their weak affinity for the cell membrane, dextran- or polymer-coated nanoparticles would take a lot longer to achieve comparable uptake. After one hour of treatment, 20% of the lower-concentration cells turned necrotic, while 60% of the higher-concentration cells did the same. Thus, the dose-dependent thermal effect directly translates to dose-dependent cytotoxicity. In research conducted by Padwal *et al.*, biocompatible citric acid-coated iron oxide nanoparticles synthesized *via* coprecipitation were shown to enhance the uptake of existing anti-TB drugs and could be a viable strategy for TB treatment.[30] The uptake of these nanoparticles by *M. smegmatis* was found to be concentration-dependent, up to 32 μg mL^{-1}. The presence of CA-MNPs doubled the intracellular levels of rifampicin compared to when the drug was used alone. Similarly, reactive oxygen species (ROS) levels, indicative of intracellular isoniazid, were higher in cells treated with both nanoparticles and isoniazid than with the drug alone.[30] Another example was provided by Gifford *et al.*, who showed that the Small Molecule Variable Ligand Display (SMLVD) approach for finding nanoparticle antibiotics could be expanded around a ligand feed ratio parameter space to find gold nanoparticle conjugates that are highly effective growth inhibitors for mycobacteria.[31] Compared to encapsulated nanoparticles, our multi-core constructs have several advantages. The lack of a matrix and the ensuing close contact between the individual cores promote cooperative behavior, which increases the global magnetic moment while preserving superparamagnetic characteristics and exceptional colloidal stability. The multi-core nanoparticle suspensions presented here have additional benefits beyond the new understanding of collective magnetic behavior. Specifically, the citrate coating offers unique advantages for cell labeling, and the collective effects modify the dynamics of the magnetic moment in a way that enhances both longitudinal and transverse relaxivities.[32]

Isoniazid in this context has a very long history of over 60 years as an irreplaceable first-line TB antibiotic engaged in both intensive and continuation phases of therapy.[33] However, the incidence of drug-resistant TB is rising. According to recent statistics, in Eastern Europe, one in three TB cases is resistant to INH, compared to one in seven cases in other regions.[34] This highlights the crucial need for new strategies to tackle resistant organisms. To tackle resistance, it is essential to understand the function of the drug. Generally, INH is a prodrug that enters the cytoplasm of mycobacterium through passive diffusion and gets activated by the enzyme KatG.[35] KatG activates INH through peroxidation, producing intracellular reactive INH-derived species. Various oxidants, such as superoxide, hydrogen peroxide, and simple alkyl hydroperoxides, facilitate this process.[35] This activation generates oxygen- and carbon-centered free radicals, which are hypothesized to be crucial for mycobacterial cell killing by damaging lipids, proteins, and nucleic acids.[35] Despite this, the discovery that INH inhibits cell wall lipid synthesis by forming inhibitory adducts with NAD+/NADP+ shifted research focus away from this mechanism.[36] Interestingly, *M. smegmatis* mutants lacking mycothiol synthesis, an important antioxidant in *M. tuberculosis*, showed increased resistance to INH but heightened sensitivity to other oxidants, suggesting a complex role for INH-derived radicals.[36] Therefore, the appropriate mechanism of action of isoniazid is yet to make convincing progress since it requires combinational approaches of bacterial genetics, biochemical works, and detailed free radical chemistry.[37] Looking ahead the nanotechnology-based approach of constituting engineered nanoparticles might act in combination as a potent antituberculosis cocktail and would be able to attack multiple targets.

4.1. Proposed mechanism of the assembled nanoconjugate antimicrobial activity

From our experimental analysis, we infer that MC-IONPs could be an excellent drug delivery agent. We analysed the effect of INH–MC-IONPs on different phases of bacteria, *i.e.* replicating, biofilm, persistent, and dormancy phases. Among these phases, dormancy of mycobacterium species is the most challenging to tackle. INH is particularly ineffective against dormant bacteria. Our data reveal the excellent activity of INH–MC-IONPs comparatively at lower doses than that of INH. However,

it is still not robust enough to tackle the dormant mycobacterial species effectively.

The interaction of INH–MC-IONPs with the bacterial membrane triggers a series of thermodynamical and physiochemical reactions, which in turn alter the membrane surface tension, generating mediated chemical modifications of accessible functional groups of the membrane. Henceforth, the interactions between the assembled INH at the MC-IONP interface play an important role in determining the antibacterial propensity of the conjugates compared to the individual entity.

M. smegmatis comprised of a thick waxy cell wall rich in mycolic acid is more complex than typical Gram-positive organisms. Although *M. smegmatis* does have an overall negative surface charge due to the presence of acidic phospholipids; however, the lipid-rich outer membrane is highly impermeable to many substances including nanoparticles, thereby preventing the effective penetration between the negatively charged MC-IONPs even at millimolar concentration,[38] whereas on the other hand using nanoparticles in combination with agents that can weaken or disrupt mycobacterial cell walls enhances the overall antimicrobial effect. In contrast, INH disrupts the synthesis of both mycolic acids and nucleic acids. It was discovered that INH oxidation in the presence of NADH and InhA produced potent covalent INH–NADH adducts, which are InhA inhibitors. An enoyl acyl carrier protein reductase called InhA participates in the production of mycolic acids, so its inhibition is consistent with mycobacteria's particular susceptibility to INH.[39] It was subsequently demonstrated that these adducts could develop during INH oxidation when NADH is present in free solution by Minisci introducing the isonicotinoyl radical into NAD. This happens at roughly 10^6 M^{-1} s^{-1}.[40] The metabolic consequences of NADH/NAD+ ratios on INH sensitivity in mycobacteria provide more evidence for the role of NAD+ in the production of INH–NAD adducts wherein decreased levels of NAD+ conferred INH resistance, as well as *via* changes to the NADH oxidase gene and in some isolates resistant to INH. Adducts of INH-NAD that can inhibit InhA are produced in simple KatG-catalysed reactions.[41] Also, the INH–NADP adducts strongly inhibit MAbA, which is an NADPH-dependent ketoacyl-ACP reductase that is also central to mycolic acid synthesis. Thus, INH adducts of both NAD+ and NADP+ could inhibit different steps in cell wall lipid synthesis.[41]

The physicochemical properties of MC-IONP assist in further permeabilization of the conjugate through the ROS-mediated change in the bacterial membrane surface. The non-covalent interaction arising from different functional groups present over the conjugate interface and bacterial membrane cooperatively generates a significant amount of energy to catalyze the conjugate permeabilization process. Different physicochemical properties of the membrane interface, like (i) stretching and elasticity of the membrane, (ii) thermal fluctuation of the cell membrane, and (iii) hydrophobic exclusion of polar surfaces by the membrane, will resist the conjugate against permeabilization. However, microscopy data indicated that the conjugate interactions with the membrane interface generate a sufficient amount of energy to help the permeabilization without splitting the conjugate. The increase in surface tension with time at the loci of adhesion of the INH–MC-IONP conjugate and membrane causes the conjugate's invagination, leaving behind the pore/cavity of respective size (Fig. 7). The cavity(s) results in the rapid efflux of the vital cellular moieties leading to loss of cell viability. Upon internalization of the conjugate, the conjugate kills the bacteria by targeting and damaging various intracellular biomolecules in the

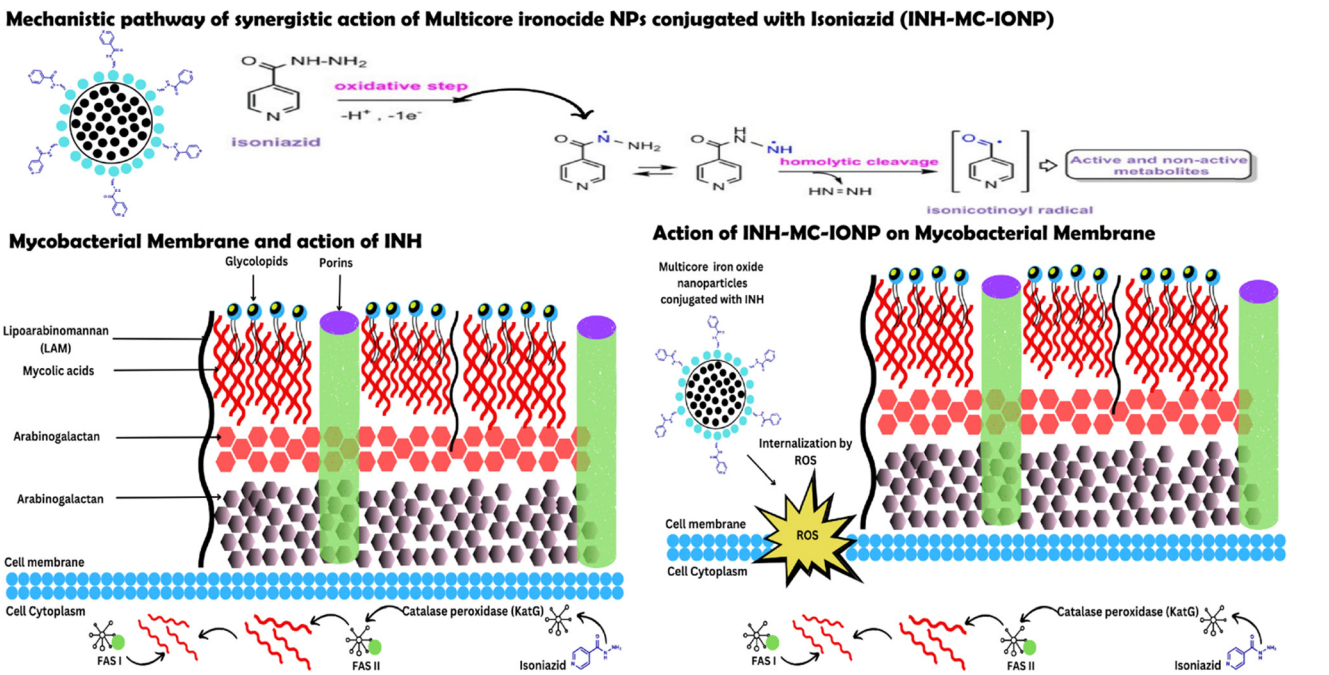

Fig. 10 Mechanistic action of INH–MC-IONPs on *M. smegmatis*.

ROS-mediated pathway, in addition to the INH mediated cell death. The data, together, indicated that, besides the broadening of INH activity against *M. smegmatis* at sub-micromolar concentrations, the MC-IONP interface enhances the efficiency of of the INH assembly. Hence, the interfacial assembly of INH at the MC-IONP interface enhances the antimycobacterial efficacy, Fig. 10. Findings from the study reveal that electrostatic interactions play an important role in the interfacial assembly of INH at the MC-IONP interface, forming stable conjugates. The interfacial assembly is confirmed by the change in the nanoparticle's specific SPR signature, IR signatures for metals and bonds, and surface potential neutralization. Additionally, the interaction energy and interfacial ROS generation play an important role in destabilizing the membrane to favor the conjugate permeabilization process. The cavity formed in the membrane on the permeabilization and the intracellular ROS generation, primarily, results in the cell's non-viability. Hence, this conjugate can be adopted as a potential antibacterial formulation to broaden the efficacy of INH.

5. Conclusions

The current study employs the use of the electrostatic assembly method to easily conjugate the first-line TB medication isoniazid onto the surface of MC-IONPs that have been citrate-grafted. Furthermore, the pore generation mechanism in the cell membrane is responsible for the major antibacterial mechanism of the nanoconjugate. The INH–MC-IONP nanoconjugate's ROS-dependent killing mechanism is demonstrated by the MIC and MBC growth kinetics experiment. A methodical approach to the study has shown that the nanoconjugate's minimum dosage is highly efficient against *M. smegmatis* reproducing, biofilm, and persistent models. The study even concentrated on the nanocomposite's cytotoxicity, which showed that the INH–MC-IONP nanoconjugate has no toxicity up to 25 mg mL^{-1}. Future research should concentrate on using this nanoconjugate against different infections and developing more standardized biocompatibility testing for use in a variety of applications.

Author contributions

Lipsa Leena Panigrahi – conceptualization, experimentation, writing of manuscript; Ashirbad Sarangi – experimentation; Bhabani Shankar Das – experimentation; Shashank Shekhar – experimentation; Debapriya Bhattacharya – editing; Manoranjan Arakha – conceptualization, formal analysis, supervision, final editing.

Conflicts of interest

There are no conflicts to declare.

Data availability

All data described in this study are contained within the main article.

References

1 J. L. Khawbung, D. Nath and S. Chakraborty, Drug resistant Tuberculosis: A review, *Comp. Immunol., Microbiol. Infect. Dis.*, 2021, **74**, 101574.
2 A. Matteelli, *et al.*, Multidrug-resistant and extensively drug-resistant Mycobacterium tuberculosis: epidemiology and control, *Expert Rev. Anti-Infect. Ther.*, 2007, **5**(5), 857–871.
3 J. Azuma, *et al.*, NAT2 genotype guided regimen reduces isoniazid-induced liver injury and early treatment failure in the 6-month four-drug standard treatment of tuberculosis: a randomized controlled trial for pharmacogenetics-based therapy, *Eur. J. Clin. Pharmacol.*, 2013, **69**, 1091–1101.
4 V. Dartois and T. Dick, Therapeutic developments for tuberculosis and nontuberculous mycobacterial lung disease, *Nat. Rev. Drug Discovery*, 2024, **23**(5), 381–403.
5 M. Park, G. Satta and O. M. Kon, An update on multidrug-resistant tuberculosis, *Clin. Med.*, 2019, **19**(2), 135–139.
6 N. Larson and H. Ghandehari, Polymeric conjugates for drug delivery, *Chem. Mater.*, 2012, **24**(5), 840–853.
7 V. F. Cardoso, *et al.*, Advances in magnetic nanoparticles for biomedical applications, *Adv. Healthcare Mater.*, 2018, **7**(5), 1700845.
8 M. Sedlák, *et al.*, Synthesis and characterization of a pH-sensitive conjugate of isoniazid with Fe3O4@ SiO2 magnetic nanoparticles, *Bioorg. Med. Chem. Lett.*, 2013, **23**(16), 4692–4695.
9 H. H. Gustafson, *et al.*, Nanoparticle uptake: the phagocyte problem, *Nano Today*, 2015, **10**(4), 487–510.
10 G. De Crozals, *et al.*, Nanoparticles with multiple properties for biomedical applications: A strategic guide, *Nano Today*, 2016, **11**(4), 435–463.
11 P. Hugounenq, *et al.*, Iron oxide monocrystalline nanoflowers for highly efficient magnetic hyperthermia, *J. Phys. Chem. C*, 2012, **116**(29), 15702–15712.
12 S. J. Iyengar, *et al.*, Magnetic, X-ray and Mössbauer studies on magnetite/maghemite core–shell nanostructures fabricated through an aqueous route, *RSC Adv.*, 2014, **4**(110), 64919–64929.
13 L. Li, *et al.*, Effect of synthesis conditions on the properties of citric-acid coated iron oxide nanoparticles, *Microelectron. Eng.*, 2013, **110**, 329–334.
14 Z. N. Kayani, *et al.*, Synthesis of iron oxide nanoparticles by sol–gel technique and their characterization, *IEEE Trans. Magn.*, 2014, **50**(8), 1–4.
15 P. Kucheryavy, *et al.*, Superparamagnetic iron oxide nanoparticles with variable size and an iron oxidation state as prospective imaging agents, *Langmuir*, 2013, **29**(2), 710–716.
16 C. Anzivino and A. Zaccone, Molecular-Level Relation between the Intraparticle Glass Transition Temperature and the Stability of Colloidal Suspensions, *J. Phys. Chem. Lett.*, 2023, **14**(39), 8846–8852.
17 L. Zhou, *et al.*, Characteristics of equilibrium, kinetics studies for adsorption of Hg (II), Cu (II), and Ni (II) ions by thiourea-modified magnetic chitosan microspheres, *J. Hazard. Mater.*, 2009, **161**(2–3), 995–1002.

18 T. Krasia-Christoforou, *et al.*, From single-core nanoparticles in ferrofluids to multi-core magnetic nanocomposites: Assembly strategies, structure, and magnetic behavior, *Nanomaterials*, 2020, **10**(11), 2178.
19 F. Ahrentorp, *et al.*, Effective particle magnetic moment of multi-core particles, *J. Magn. Magn. Mater.*, 2015, **380**, 221–226.
20 J. Nowak-Jary and B. Machnicka, In vivo biodistribution and clearance of magnetic iron oxide nanoparticles for medical applications, *Int. J. Nanomed.*, 2023, 4067–4100.
21 S. Tiwari, *et al.*, Macrophage-specific targeting of isoniazid through mannosylated gelatin microspheres, *AAPS PharmSciTech*, 2011, **12**, 900–908.
22 S. Gunasekaran and S. Ponnusamy, Vibrational spectra and normal coordinate analysis of isoniazid, *Indian J. Phys.*, 2005, **79**(2), 171–175.
23 K. Iqbal, *et al.*, Isoniazid conjugated magnetic nanoparticles loaded with Amphotericin B as a potent Antiamoebic agent against Acanthamoeba castellanii, *Antibiotics*, 2020, **9**(5), 276.
24 I. L. Sparks, *et al.*, Mycobacterium smegmatis: the vanguard of mycobacterial research, *J. Bacteriol.*, 2023, **205**(1), e00337.
25 J. V. Jokerst and S. S. Gambhir, Molecular imaging with theranostic nanoparticles, *Acc. Chem. Res.*, 2011, **44**(10), 1050–1060.
26 A. Vassallo, *et al.*, Nanoparticulate antibiotic systems as antibacterial agents and antibiotic delivery platforms to fight infections, *J. Nanomater.*, 2020, **2020**(1), 6905631.
27 V. Agrahari and V. Agrahari, Facilitating the translation of nanomedicines to a clinical product: challenges and opportunities, *Drug Discovery Today*, 2018, **23**(5), 974–991.
28 C. Blanco-Andujar, *et al.*, High performance multi-core iron oxide nanoparticles for magnetic hyperthermia: microwave synthesis, and the role of core-to-core interactions, *Nanoscale*, 2015, **7**(5), 1768–1775.
29 L. Lartigue, *et al.*, Cooperative organization in iron oxide multi-core nanoparticles potentiates their efficiency as heating mediators and MRI contrast agents, *ACS Nano*, 2012, **6**(12), 10935–10949.
30 P. Padwal, R. Bandyopadhyaya and S. Mehra, Biocompatible citric acid-coated iron oxide nanoparticles to enhance the activity of first-line anti-TB drugs in Mycobacterium smegmatis, *J. Chem. Technol. Biotechnol.*, 2015, **90**(10), 1773–1781.
31 J. C. Gifford, *et al.*, Thiol-modified gold nanoparticles for the inhibition of Mycobacterium smegmatis, *Chem. Commun.*, 2014, **50**(100), 15860–15863.
32 H. Lee, *et al.*, Recent developments in magnetic diagnostic systems, *Chem. Rev.*, 2015, **115**(19), 10690–10724.
33 P. Padwal, *et al.*, Biocompatible citric acid-coated iron oxide nanoparticles to enhance the activity of first-line anti-TB drugs in Mycobacterium smegmatis, *J. Chem. Technol. Biotechnol.*, 2015, **90**(10), 1773–1781.
34 A. Dadu, *et al.*, Drug-resistant tuberculosis in eastern Europe and central Asia: a time-series analysis of routine surveillance data, *Lancet Infect. Dis.*, 2020, **20**(2), 250–258.
35 A. N. Unissa, *et al.*, Overview on mechanisms of isoniazid action and resistance in Mycobacterium tuberculosis, *Infect., Genet. Evol.*, 2016, **45**, 474–492.
36 C. Vilchèze, J. Jacobs and R. William, The mechanism of isoniazid killing: clarity through the scope of genetics, *Annu. Rev. Microbiol.*, 2007, **61**(1), 35–50.
37 S. S. Swain, *et al.*, Molecular mechanisms of underlying genetic factors and associated mutations for drug resistance in Mycobacterium tuberculosis, *Emerging Microbes Infect.*, 2020, **9**(1), 1651–1663.
38 S. M. Batt, D. E. Minnikin and G. S. Besra, The thick waxy coat of mycobacteria, a protective layer against antibiotics and the host's immune system, *Biochem. J.*, 2020, **477**(10), 1983–2006.
39 X. He, A. Alian and P. R. O. De Montellano, Inhibition of the Mycobacterium tuberculosis enoyl acyl carrier protein reductase InhA by arylamides, *Bioorg. Med. Chem.*, 2007, **15**(21), 6649–6658.
40 M. Nguyen, *et al.*, Mn (III) pyrophosphate as an efficient tool for studying the mode of action of isoniazid on the InhA protein of Mycobacterium tuberculosis, *Antimicrob. Agents Chemother.*, 2002, **46**(7), 2137–2144.
41 C. Vilcheze, *et al.*, Altered NADH/NAD+ ratio mediates coresistance to isoniazid and ethionamide in mycobacteria, *Antimicrob. Agents Chemother.*, 2005, **49**(2), 708–720.